ORIGINAL RESEARCH

Self-Amplified pH/ROS Dual-Responsive Co-Delivery Nano-System with Chemo-Photodynamic Combination Therapy in Hepatic Carcinoma Treatment

Yu Huang [1],*, Shuyang Wu [1],*, Jingjing Li[1,2], Chenglin He[1], Yanfen Cheng[3], Nan Li [1], Yitao Wang[1,4], Yihan Wu[1], Jinming Zhang [1]

[1]State Key Laboratory of Southwestern Chinese Medicine Resources, School of Pharmacy, Chengdu University of Traditional Chinese Medicine, Chengdu, People's Republic of China; [2]Department of Rehabilitation Sciences, Faculty of Health and Social Sciences, Hong Kong Polytechnic University, Hong Kong, SAR, People's Republic of China; [3]Chengdu University, Chengdu, People's Republic of China; [4]Macau Center for Research and Development in Chinese Medicine, State Key Laboratory of Quality Research in Chinese Medicine, Institute of Chinese Medical Sciences, University of Macau, Macau, People's Republic of China

*These authors contributed equally to this work

Correspondence: Jinming Zhang; Yihan Wu, State Key Laboratory of Southwestern Chinese Medicine Resources, School of Pharmacy, Chengdu University of Traditional Chinese Medicine, Chengdu, People's Republic of China, Email cdutcmzjm@126.com; yihanwuone@126.com

Background: Chemo-photodynamic combination therapy has demonstrated significant potential in the treatment of cancer. Triptolide (TPL), a naturally derived anticancer agent, when combined with the photosensitizer Chlorin e6 (Ce6), has shown to provide enhanced anti-tumor benefits. However, the development of stimuli-responsive nanovehicles for the co-delivery of TPL and Ce6 could further enhance the efficacy of this combination therapy.

Methods: In this study, we synthesized a pH/ROS dual-responsive mPEG-$_{TK}$-PBAE copolymer, which contains a pH-sensitive PBAE moiety and a ROS-sensitive thioketal (TK) linkage. Through a self-assembly process, TPL and Ce6 were successfully co-loaded into mPEG-$_{TK}$-PBAE nanoparticles, hereafter referred to as TPL/Ce6 NPs. We evaluated the pH- and ROS-sensitive drug release and particle size changes. Furthermore, we investigated both the in vitro suppression of cellular proliferation and induction of apoptosis in HepG2 cells, as well as the in vivo anti-tumor efficacy of TPL/Ce6 NPs in H22 xenograft nude mice.

Results: The mPEG-$_{TK}$-PBAE copolymer was synthesized through a one-pot Michael-addition reaction and successfully co-encapsulated both TPL and Ce6 by self-assembly. Upon exposure to acid pH values and high ROS levels, the payloads in TPL/Ce6 NPs were rapidly released. Notably, the abundant ROS generated by the released Ce6 under laser irradiation further accelerated the degradation of the nanosystem, thereby amplifying the tumor microenvironment-responsive drug release and enhancing anticancer efficacy. Consequently, TPL/Ce6 NPs significantly increased PDT-induced oxidative stress and augmented TPL-induced apoptosis in HepG2 cells, leading to synergistic anticancer effects in vitro. Moreover, administering TPL/Ce6 NPs (containing 0.3 mg/kg of TPL and 4 mg/kg of Ce6) seven times, accompanied by 650 nm laser irradiation, efficiently inhibited tumor growth in H22 tumor-bearing mice, while exhibiting lower systemic toxicity.

Conclusion: Overall, we have developed a tumor microenvironment-responsive nanosystem for the co-delivery of TPL and Ce6, demonstrating amplified synergistic effects of chemo-photodynamic therapy (chemo-PDT) for hepatocellular carcinoma (HCC) treatment.

Keywords: triptolide, PDT, ROS, Ce6, pH responsive, hepatic carcinoma

Introduction

Hepatocellular carcinoma (HCC), the most prevalent form of primary liver cancer, ranks as the third leading cause of cancer-related deaths and poses a significant global health challenge. Despite the availability of FDA-approved anti-HCC

agents such as sofitinib and anti-PD-1/PD-L1 monoclonal antibodies, as well as traditional chemotherapeutic drugs like doxorubicin, therapeutic outcomes remain unsatisfactory, particularly for patients with unresectable HCC. Recent strategies combining photodynamic therapy (PDT) with chemotherapy have shown promise in combating HCC.[1,2] Compared to single-agent therapy, this chemo-photodynamic approach has achieved improved therapeutic outcomes with fewer side effects.[3] Successful initiatives have demonstrated the synergistic anti-HCC effects of a photosensitizer with paclitaxel and anti-PD-L1 combination.[1] Furthermore, Weinire Abuduwaili et al have developed an iridium-based photosensitizer combined with sorafenib, offering synergistic benefits for HCC treatment through chemo-photodynamic therapy.[2] Yet, innovative therapies that effectively combat HCC while minimizing side effects are still needed.

Triptolide (TPL), a diterpenoid extracted from the medicinal herb *Tripterygium wilfordii* Hook. F., is known for its broad-spectrum anti-tumor properties, including apoptosis induction through p53 activation, modulation of the c-Myc/miRNA clusters/target genes axis,[4] and inhibition of TNF/NF-κB/BCL2 signaling.[5] Significantly, TPL has shown greater efficacy against a range of HCC cell lines compared to commonly used anti-HCC drugs like doxorubicin and sorafenib.[6,7] However, its potential to cause liver damage severely limits its clinical use. Reducing the dosage and enhancing tumor-targeted delivery of TPL are critical strategies to improve its anti-tumor effectiveness and reduce side effects. Recent studies have explored combining TPL with other anticancer agents using nanocarrier co-encapsulation for tumor treatment.[8,9] The combination of TPL and Ce6 for chemo-photodynamic therapy remains highly promising.[10] The strategy of co-delivering multiple therapeutic agents within a single nanocarrier has emerged as a promising approach to enhance tumor targeting. Yu et al designed a light-activatable liposome encapsulating both Ce6 and TPL, where Ce6-generated ROS under laser irradiation oxidizes the liposome's unsaturated phospholipids, facilitating the release of TPL.[11] However, achieving selective and rapid payload release in tumor cells through phospholipid oxidation remains challenging.

In light of the tumor microenvironment's (TME) unique characteristics, TME-responsive nanocarriers that respond to acidic pH, elevated ROS and glutathione levels, hypoxia, and overexpressed enzymes offer promising avenues for targeted, on-demand drug release.[12–14] Leveraging the acidic pH-responsive properties of poly (β-amino ester)(PBAEs), we have developed an acidic pH-sensitive nanosystem for delivering TPL alone[15] or in combination with Ce6,[16] thereby enhancing the synergistic therapeutic effects through pH-sensitive drug release. Moreover, evidence suggests that nanoparticles responsive to multiple stimuli can achieve more precise, on-demand release at the target site, significantly enhancing treatment efficacy.[17–23] The high ROS concentrations in tumors, which can be up to a thousand times higher than in normal cells, present an ideal target for constructing ROS-responsive drug delivery systems.[24]

Additionally, the heterogeneity of tumors, encompassing various regions of tumor tissue and different stages of tumor cells, results in fluctuating endogenous ROS levels within tumor cells. To address this challenge, some strategies have employed ROS-generating agents to elevate intra-tumoral ROS levels.[25] In this study, we developed a self-amplifying pH/ROS dual-responsive nanovesicle, composed of PBAE-based copolymers (mPEG-TK-PBAE), for the co-delivery of TPL and Ce6 (TPL/Ce6 NPs) aimed at chemo-PDT for HCC (Scheme 1). The designed nanoparticles specifically accumulate in tumor, where high levels of intracellular ROS and low pH values in endosomes/lysosomes trigger the rapid disintegration of TPL/Ce6 NPs, due to the cleavage of the TK linkage and protonation of the PBAE core. Upon 650 nm laser irradiation, Ce6-generated ROS further accelerates the release of payloads, acting as a ROS amplifier. Consequently, TPL/Ce6 NPs synergistically enhance ROS-mediated cell death, leading to improved anticancer outcomes through the co-delivery of TPL and Ce6 in this self-amplified pH/ROS nanosystem.

Materials and Methods
Materials
Chlorin e6 (Ce6, purity ≥98%), triptolide (TPL, purity ≥98%), methoxy PEG, and 4-amino-1-butanol were acquired from Macklin Co., Ltd. (Shanghai, China). The CCK-8 kit was obtained from Bioground Co., Ltd. (Chongqing, China). DCFH-DA and Annexin V-FITC/PI kits were sourced from Thermo Fisher Scientific Co., Ltd. Human hepatocarcinoma cell lines (HepG2 cell) and mouse hepatocarcinoma cell lines (H22 cell) were procured from the Chinese Academy of Medical Sciences Co., Ltd. (Shanghai, China). Male ICR mice (4 weeks of age, 20–25 g) and nude mice (4 weeks of age, 18–20 g) were purchased from SPF Biotechnology Co. Ltd. (Beijing, China). All animal experiments were approved by
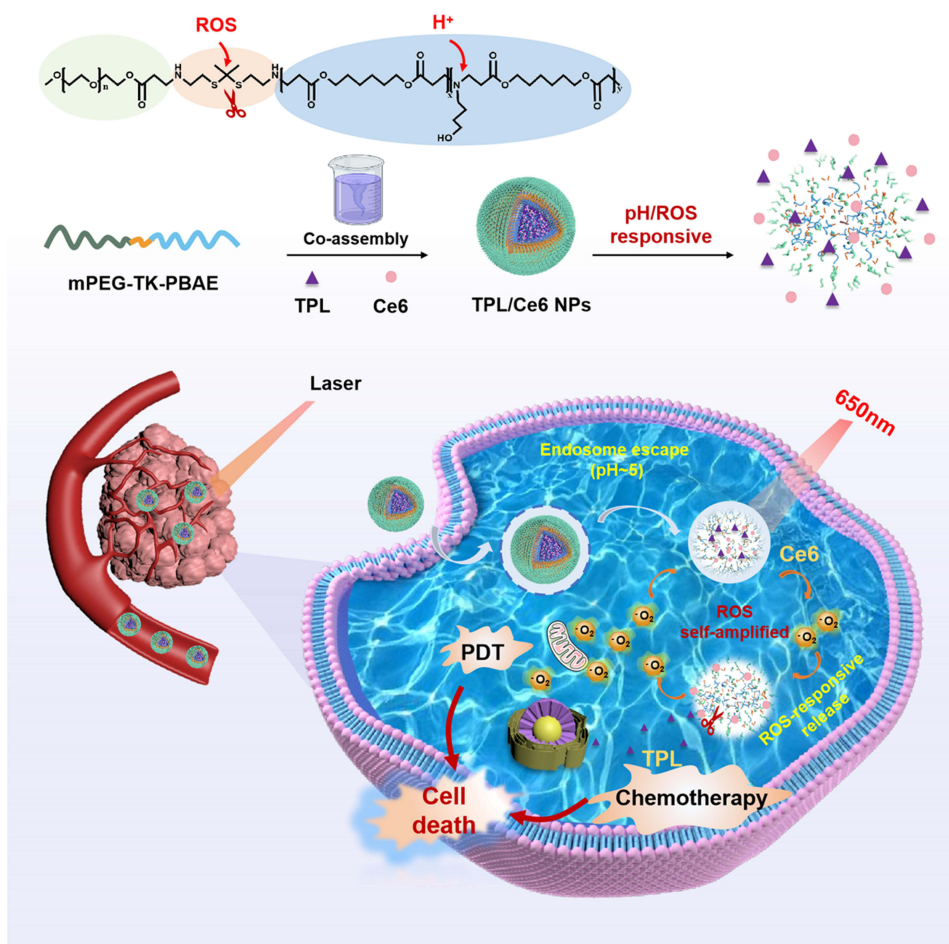
Scheme 1 Schematic representation of self-assembly of TPL/Ce6 NPs and dual-synergistic combination therapy of chemotherapy and PDT.

the ethics committee of the "Experimental Animals Administrative Committee of Chengdu University of Traditional Chinese Medicine" (Chengdu, China) and were conformed to the Guidelines for the Care and Use of Laboratory Animals published by the National Institutes of Health, USA. Animal welfare was ensured in all animal experiments (permission number: SYXK2020-124). All animals were acclimated for a minimum of 7 days prior to experimentation and housed under a 12/12-h light/dark cycle, with up to five animals per cage and unlimited access to food and water.

Synthesis and Characterization of mPEG-_{TK}-PBAE Triblock Co-Polymer

Anhydrous toluene (25 mL), acryloyl chloride (6 mmol, 0.49 mL), and triethylamine (TEA, 18 mmol, 2.5 mL) were combined dropwise in a two-neck flask containing mPEG (2 mmol). The reaction proceeded at 45°C for 15 h. Following the reaction, the insoluble triethylamine hydrochloride salt was removed by filtration, yielding acrylated mPEG through precipitation in ether, which was then oven-dried.

Cysteamine hydrochloride was dissolved in hydrochloric acid (4 mL). A mixture of acetone (269 mmol) and chloroform (4 mL) was gradually added to this solution dropwise and maintained at 0°C for 12 hours until a white solid formed. This white solid was washed with chloroform, dissolved in methanol, and precipitated with anhydrous ether. Recrystallization occurred in a refrigerator at −20°C. After filtration to remove the solvent, the solid was dissolved, reacted with 1 M NaOH, and left overnight. It was then extracted thrice with dichloromethane, with the aqueous layer being collected. Anhydrous magnesium sulfate was added to the extraction solution, stirred for 3 hours, filtered, and the TK product was oven-dried.

The mPEG-$_{TK}$-PBAE amphiphilic block copolymer was synthesized via Michael addition involving mPEG, TK, HDD, and 4-amino-1-butanol. Initially, these components were dissolved in chloroform, and the reaction proceeded at 55°C for 24 h under N$_2$. Following the reaction, the mixture was transferred to a beaker, vacuum-dried, yielding the mPEG-$_{TK}$-PBAE amphiphilic block copolymer. This copolymer was further purified by precipitation in diethyl ether and vacuum drying. The structure of the copolymer was characterized using ^{1}H NMR.

Preparation and Characterization of TPL/Ce6 NPs

TPL/Ce6 NPs were fabricated using a straightforward nanoprecipitation method, relying on self-assembly in an aqueous environment. In brief, 4.2 mg of Ce6, 0.7 mg of TPL, and 20 mg of the mPEG-$_{TK}$-PBAE copolymer were co-dissolved in tetrahydrofuran (THF), then the solution was combined with water. After stirring for 2 hours at room temperature, the THF was removed using a vacuum rotary evaporator at 40°C. The resulting solution was then filtered through a 0.45 μm membrane filter and stored at 4°C in the dark.

The particle size and zeta potential of the TPL/Ce6 NPs were determined in water using a Zetasizer Nano ZSP instrument. Morphological analysis was performed with a transmission electron microscope (JEOL JEM 1200EX) at 200kv, after negative staining with phosphotungstic acid. To assess stability, three batches of TPL/Ce6 NPs were stored at 4°C, and particle size was monitored daily for one week. The concentrations of TPL and Ce6 were quantified by HPLC, using mobile phases of water and methanol (53:46, v/v) and (10:90, v/v) at measurement wavelengths of 220 and 450 nm, respectively. The entrapment efficiency (EE%) and drug-loading efficiency (DL%) of TPL and Ce6 were computed as follows:

$$EE\% = \frac{\text{the encapsulated TPL/Ce6}}{\text{free TPL/Ce6 + the encapsulated TPL/Ce6}} \times 100\%$$

$$DL\% = \frac{\text{the weight of the encapsulated TPL/Ce6}}{\text{the weight of liposomes}} \times 100\%$$

Chemical analysis of the materials, including TPL, Ce6, mPEG-$_{TK}$-PBAE, and freeze-dried TPL/Ce6 NPs, was conducted using attenuated total reflection Fourier transform infrared (ATR-FTIR) spectroscopy (AVAVCE NEO 700 MHz). All FTIR spectra were collected between 4000–600 cm^{-1} with 32 scans at a resolution of 4 cm^{-1}.

Singlet Oxygen Generation and Drug Release Behavior

To assess singlet oxygen generation, 25 μL of 50 μM SOSG was introduced into solutions of TPL/Ce6 NPs at pH 7.4, pH 5.8, and pH 5.8 with 10 mM H$_2$O$_2$, followed by illumination with a 650 nm laser at 0.63 W/cm^2 for varying durations. The concentrations of TPL and Ce6 were maintained at 40 μg/mL and 180 μg/mL, respectively. The presence of oxidized SOSG was detected using a fluorescence spectrophotometer, with a blank aqueous solution acting as a negative control.

For drug release studies, 2 mL of TPL/Ce6 NPs suspension was enclosed in a dialysis bag (MW cutoff, 5000) containing 50 mL of PBS (at pH 5.8 or 7.4 with 10 mM H$_2$O$_2$) and subjected to dialysis at 37°C and 120 rpm in an oscillating incubator. Samples of 1 mL were collected periodically, with an equivalent volume of fresh dialysis medium added. Drug release rates were determined by HPLC, and cumulative release was calculated.

Cellular Uptake in vitro

The internalization of TPL/Ce6 NPs by HepG2 cells was examined using flow cytometry and confocal microscopy. HepG2 cells were seeded in 24-well plates and incubated overnight. The medium was replaced with solutions of free TPL, free Ce6 (54 nM), and TPL/Ce6 NPs for 1, 2, 4, and 8 h. Post-incubation, the cells were fixed, stained, washed, and imaged with CLSM to observe the intracellular distribution and uptake of TPL/Ce6 NPs. Flow cytometry quantified the uptake of TPL/Ce6 NPs in HepG2 cells.

TPL/Ce6 NPs Cytotoxicity Against HCC Cancer Cells

The cytotoxicity of TPL/Ce6 NPs towards HepG2 cells was evaluated using the CCK 8 kit. HepG2 cells (6.0 ×10^4 cells/ mL) were cultured in a 96-well plate and exposed to TPL/Ce6 NPs (pH 7.4, or pH 5.8, 10 mM H$_2$O$_2$) for 48 h. A range of

concentrations of TPL (5–160 nM), Ce6 (13.5–432 nM), TPL + Ce6 (T&C, at a molar ratio of TPL/ Ce6 of 1/2.7) were applied. Cells were irradiated with a 650 nm laser at 0.63 W / cm^2 for 5 min, followed by treatment with CCK-8 solution. Absorbance was measured at 450 nm using a microplate reader. The combination index (CI) value was employed to assess the synergistic effect of TPL and Ce6 co-treatment.

Intracellular ROS Generation and Enhanced the Cell Apoptosis

HepG2 cells (2.0×10^5 cells/mL) were cultured in 24-well plates overnight. Cells were treated with free Ce6, free TPL, free Ce6+TPL (T&C), TPL/Ce6 NPs (pH 5.8), or TPL/Ce6 NPs (pH 5.8+10 mM H_2O_2). After 4 h, the medium was replaced with DCFH-DA and incubated for 20 min. Following this, cells were exposed to laser irradiation (650 nm, 0.63 W/cm^2) for 5 min. Flow cytometry quantified the DCF fluorescence of TPL/Ce6 NPs in HepG2 cells.

After overnight culture, HepG2 cells (2.0×10^5 cells/mL) were incubated with the same treatments for 4 h, followed by 5 min of laser irradiation. Cells were then incubated for an additional 48 h, stained with Annexin V-FITC/PI, and the apoptosis rate was determined via flow cytometry.

Distribution of TPL/Ce6 NPs in vivo

To assess the distribution of TPL/Ce6 NPs in vivo, tumor-bearing mice were randomly assigned and intravenously administered with either free Ce6 or TPL/Ce6 NPs (with an equal Ce6 dosage of 4 mg/kg). The IVIS Lumina Series imaging system captured images at time points of 0, 2, 4, 6, 8, 10, 12, and 24 h post-injection. Subsequently, mice were anesthetized and euthanized after a 24-h observation period, and their tumors and major organs, including the heart, lungs, liver, spleen, and kidneys, were harvested for ex vivo imaging.

Tumor Growth Inhibition in vivo

To further investigate the therapeutic efficacy, tumor-bearing mice (with tumor sizes of 140–160 mm^3) were divided into six groups: untreated control (Saline), DOX, free TPL, T&C, TPL/NPs, and TPL/Ce6 NPs. Each group received injections of the corresponding drug (0.3 mg/kg TPL and 4 mg/kg Ce6) every other day. At 3 h and 12 h post-injection, mice in the irradiation groups were exposed to laser irradiation (650 nm, 0.63 W/cm^2) for 5 min. Over a 14-day period, tumor volume and body weight were monitored bi-daily. At the study's conclusion, animals were humanely euthanized by cervical dislocation, and blood samples were collected through ocular puncture. The tumor and key organs (heart, lungs, kidneys, liver, and spleen) were excised, and tumor dimensions were recorded.

Histological analyses (H&E, Ki67, Bax, Bcl-2, CD31, and VEGF staining) were conducted to further assess tumor suppression, apoptosis, and angiogenesis inhibition. AST, ALT, BUN, and Cr levels were measured using a blood biochemical analyzer.

Statistical Analysis

All data are reported as mean ± standard deviation from three independent experiments. Statistical differences were evaluated using one-way ANOVA ($P < 0.05$, 0.01, and 0.001 were considered statistically significant and were labeled as *, **and ***respectively. NS indicated not statistical significance.)

Results

Preparation and Characterization of mPEG-$_{TK}$-PBAE Block Copolymer

Primarily, the amine-ketone condensation thiol-amine ($NH_{2-TK}-NH_2$) linkage was synthesized as per a prior study[26] (Figure S1A) and characterized by ^{1}H NMR spectroscopy (Figure S1B). The spectral signals vanished at 2.10 ppm (d') and emerged at 1.67 ppm (c'), indicating the reaction of the carbonyl group in acetone with the mercaptan in cysteamine hydrochloride. Subsequently, the amphiphilic block copolymer was synthesized through a Michael addition reaction involving the mPEG moiety, $NH_{2-TK}-NH_2$, 1,6-hexanediyl diacrylate (HDDA), and 4-amino-1-butanol (molar ratio=1:1:5:5) using a one-pot synthesis method (Figure 1A). As illustrated in Figure 1B, the signals at 1.33 ppm (j, k) in the ^{1}H NMR spectra of mPEG-$_{TK}$-PBAE corresponded to the methylene protons of 4-amino-1-butanol. The intense
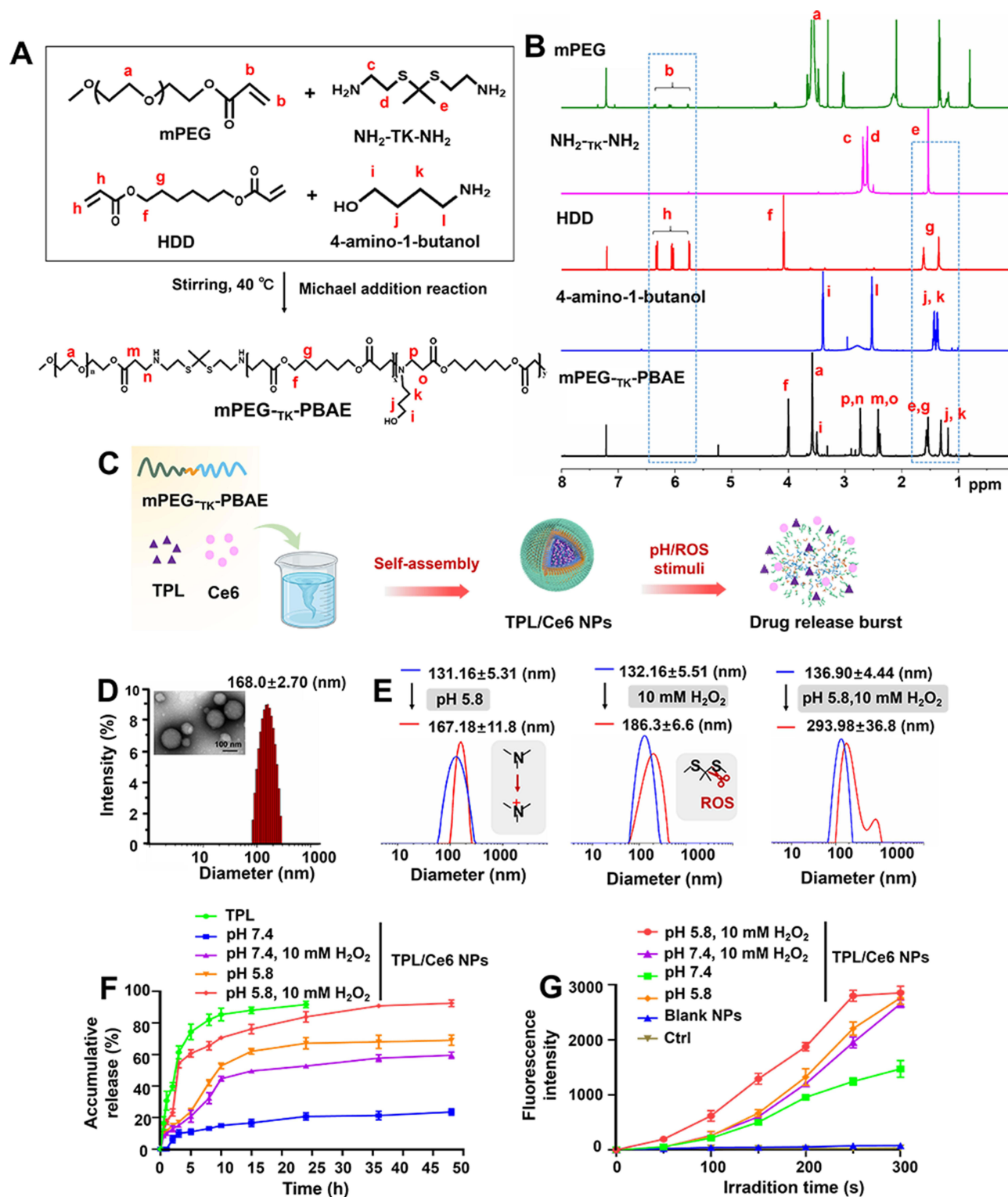
Figure 1 (**A**) Synthetic route and ¹H-NMR spectra (**B**) of mPEG-TK-PBAE copolymer (the red letters in Figure 1A represent different hydrocarbons, and the red letters in Figure 1B correspond to the hydrogen nuclear mass spectra of the hydrocarbons in Figure 1A). (**C**) Schematic diagram of the self-assembly preparation of TPL/Ce6 NPs and pH/ROS dual-responsive drug release property. (**D**) Particle size distribution determined using DLS and TEM images of TPL/Ce6 NPs. (**E**) Particle size changes in TPL/Ce6 NPs in response to acid and/or oxidant release media. pH/ROS-responsive drug release (**F**) and singlet oxygen production efficiency by SOSG probe determination (**G**) of TPL/Ce6 NPs.

peaks were no longer present at 6 ppm (b, h), while signals were observed at 2.4 ppm (m, o) and 2.7 ppm (p, n), demonstrating the complete reaction of diacrylate monomers (-CH$_2$=CH-COOR) with primary amine (-NH$_2$) and the conversion of carbon-carbon double bonds to single bonds (the red letters in Figure 1A represent different hydrocarbons, and the red letters in Figure 1B correspond to the hydrogen nuclear mass spectra of the hydrocarbons in Figure 1A). These findings confirmed the successful synthesis of the mPEG-$_{TK}$-PBAE copolymer.

## Synthesis and Characterization of TPL/Ce6 NPs

Given the amphiphilic structure of mPEG-$_{TK}$-PBAE, TPL and Ce6 were efficiently encapsulated within the particle core using the nanoprecipitation method (Figure 1C), achieving high drug entrapment efficiency (DEE) and drug loading efficiency (DLE). As depicted in Figure 1D, TPL/Ce6 NPs displayed smooth and spherical morphology with a uniform particle size of 168.0±2.70 nm. The DEE for TPL and Ce6 in TPL/Ce6 NPs was 96.47±1.76% and 96.55±1.96%, respectively, with DLE values of 4.45±0.01% for TPL and 25.39±1.33% for Ce6. The consistent size and zeta potential of TPL/Ce6 NPs over 7 days indicated excellent storage stability (Figure S2). Additionally, FT-IR spectroscopy was utilized to reveal the intermolecular interactions between the payloads and nanovesicles (Figure S3). The FT-IR spectrum of TPL showed characteristic peaks at 1721 cm^{-1} and 3455 cm^{-1}, corresponding to the carbonyl and epoxy groups on the lactone ring, respectively. The FT-IR spectrum of Ce6 featured peaks at 1711 cm^{-1} and 3293 cm^{-1}, representing the stretching vibrations of C-O and O-H, respectively. These peaks were absent in the FT-IR spectra of TPL/Ce6 NPs, indicating effective encapsulation of these agents within the NPs rather than forming a physical mixture.

Drug Release and PDT Efficiencies of TPL/Ce6 NPs

To validate the pH/ROS dual-responsive profiles of TPL/Ce6 NPs, we examined the changes in particle size and drug release under acidic and/or oxidizing conditions. Particle size expanded from 131.16 ± 5.31 nm to 167.18 ± 11.8 nm in a pH 5.8 environment and from 132.16 ± 5.51 nm to 186.3 ± 6.6 nm with 10 mM H$_2$O$_2$ alone. Under combined conditions of pH 5.8 and 10 mM H$_2$O$_2$, an increase in particle size was observed, along with the emergence of a small peak (Figure 1E). TPL encapsulated within TPL/Ce6 NPs exhibited a slower release rate compared to free TPL during the initial 20 h, with free TPL releasing approximately 85% within 10 h. In contrast, under physiological conditions (pH 7.4), TPL release from TPL/Ce6 NPs was markedly slow, with only 18% released within 20 h. While, under an acidic buffer (pH 5.8), TPL released reached 52% at 10 h. However, in an acidic buffer with 10 mM H$_2$O$_2$, especially during the first 10 h, TPL release reached 70%, indicating a significant acceleration. Thus, acidic conditions (pH 5.8) or 10 mM H$_2$O$_2$ alone moderately increased particle size and expedited TPL release, while an acidic buffer containing 10 mM H$_2$O$_2$ resulted in substantial particle dissociation and drug release (Figure 1F). Moreover, the SOSG probe was employed to evaluate the PDT efficiency of TPL/Ce6 NPs in vitro (Figure 1G). The slower release from the polymeric core at pH 7.4 resulted in lower singlet oxygen production under laser irradiation, compared to the medium at pH 5.8. Additionally, the presence of oxidizing stimuli in a medium with 10 mM H$_2$O$_2$ enhanced singlet oxygen production. TPL/Ce6 NPs produced the highest level of singlet oxygen under combined acid and oxidant stimuli, aligning with their pH/ROS dual responsive nature and indicating their potential for effective payload release and singlet oxygen generation in the tumor microenvironment.

Cellular Uptake of TPL/Ce6 NPs

We explored the localization of TPL/Ce6 NPs in HepG2 cells using CLSM, focusing on the fluorescence of Ce6 (Figure 2A). Following a 4-hour treatment with free Ce6, only faint red fluorescence was detected in the cytoplasm. However, cells treated with TPL/Ce6 NPs exhibited significantly stronger intracellular red fluorescence than those treated with free Ce6, highlighting the superior intracellular uptake of TPL/Ce6 NPs. The cell nucleus and cytomembrane were stained with Hoechst and phalloidin, respectively, revealing that TPL/Ce6 NPs were primarily localized in the cytoplasm. Flow cytometry (FCM) was employed to quantitatively assess the intracellular fluorescence intensity (Figure 2B), aligning with the CLSM findings. After 4 hours of incubation, TPL/Ce6 NPs demonstrated substantially higher intracellular internalization compared to free Ce6, with a 1.7-fold increase in intracellular fluorescence intensity relative to the control (Figure 2C). Leveraging the internalization capabilities of nanocarriers, these payloads achieved enhanced uptake by tumor cells.
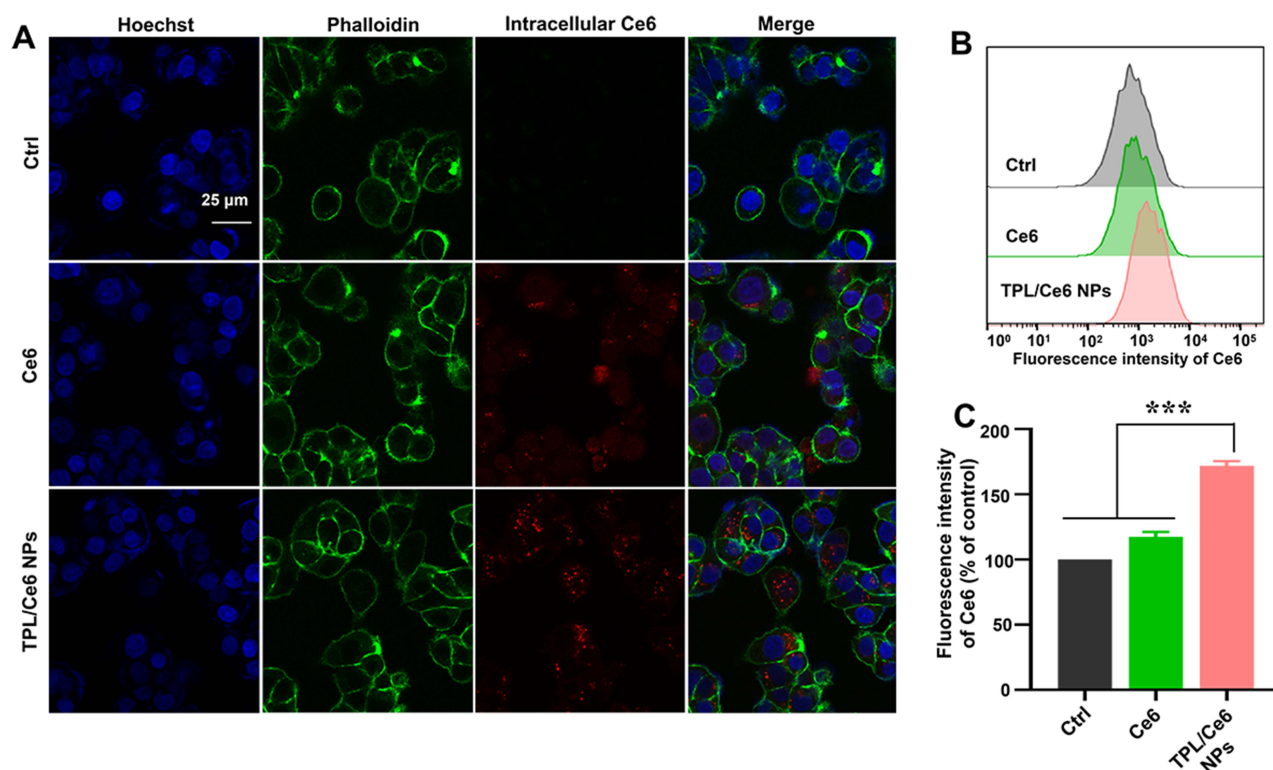
Figure 2 Cellular uptake profiles in HepG2 treatment with either free Ce6 or TPL/Ce6 NPs for 4 h. (**A**) Representative cellular uptake images by CLSM observation. Hoechst 33342 and phalloidin were employed to label cell nucleus and cytoskeleton. The scale bar is 25μm. Intracellular fluorescence intensity by FCM determination (**B**) and quantitative results (**C**). ***p < 0.001 indicates TPL/Ce6 NPs *versus* free Ce6 group.

Cytotoxicity and ROS Production Capacity of TPL/Ce6 NPs

The increased cytotoxicity of TPL/Ce6 NPs against HepG2 cells after 48 h of incubation was measured using a CCK-8 assay. Notably, monotherapy with PDT using Ce6 alone failed to significantly inhibit cell proliferation (Figure 3A). A combination of TPL and Ce6 (T&C) showed greater cytotoxicity than monotherapy with either TPL or Ce6. In contrast, TPL/Ce6 NPs markedly increased cytotoxicity, particularly in an acidic medium (pH 5.8) containing 10 mM H_2O_2, where cell viability in the TPL/Ce6 NPs group fell below 20%, indicating substantial cell mortality. The cytotoxicity of TPL/Ce6 NPs against HepG2 cells under pH/ROS dual stimuli was significantly higher than that in normal culture medium (pH 7.4). Moreover, the capacity of TPL/Ce6 NPs to generate intracellular ROS was evaluated using a DCFH-DA kit, with FCM measuring the fluorescence intensity indicative of ROS production (Figure 3B). It was observed that Ce6 treatment under laser irradiation enhanced ROS levels (Figure 3C). However, at pH 7.4, the fluorescence intensity from TPL/Ce6 NPs was lower than that of the free Ce6 and T&C groups, attributable to slow drug release at neutral pH, as demonstrated in Figure 1G. Yet, when TPL/Ce6 NPs were incubated with cells in a medium (pH 5.8, 10 mM H_2O_2), the fluorescence intensity, reflecting ROS generation, was significantly higher than in the medium at pH 7.4.

TPL/Ce6 NPs Enhanced the Cell Apoptosis

Previous studies have established that the anticancer efficacy of TPL is closely associated with its ability to promote apoptosis. In this research, we assessed the apoptosis rates in HepG2 cells treated with different formulations using Annexin V-FITC/PI double staining. Following a 48-h incubation, these formulations, each containing 20 nM TPL and/or 54 nM Ce6, exhibited varying apoptosis rates as determined by FCM analysis (Figure 3D). The results indicated that TPL (20nM) augmented the apoptotic rate in HepG2 cells by 16.34%. Compared to monotherapy with TPL or Ce6, the combination of TPL and Ce6 was more effective in enhancing apoptosis, particularly in an acidic buffer (pH 5.8) with 10 mM H_2O_2, leading to a 55.33% increase in apoptosis rates in HepG2 cells, with late apoptosis representing 53.2% of this increase. While both free TPL and free Ce6 under laser irradiation were potent in inducing apoptosis independently, their physical combination did not yield a synergistic effect on apoptosis
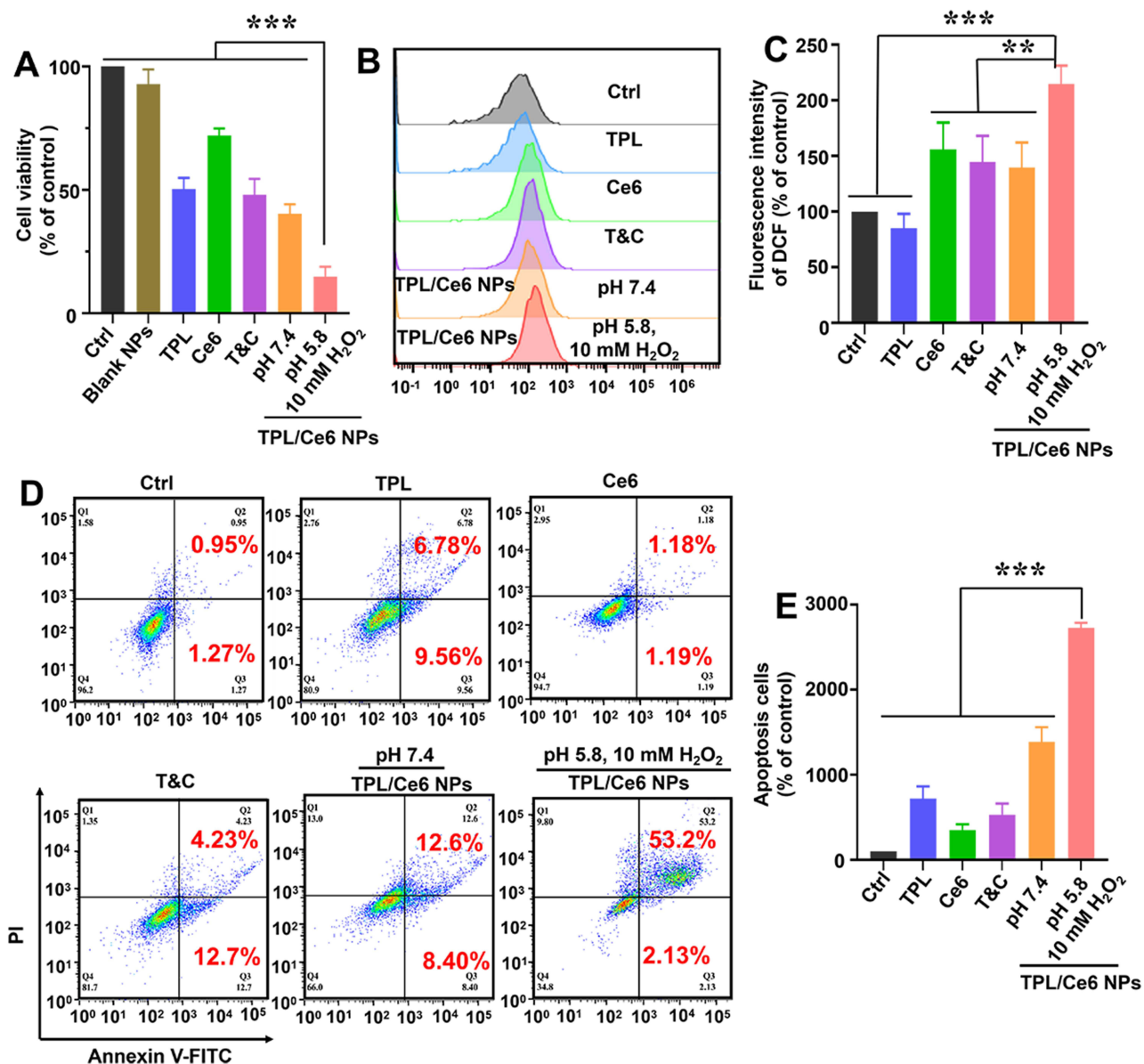
Figure 3 (**A**) Cytotoxicity of TPL/Ce6 NPs against HepG2 cells with laser irradiation after 48 h treatment. (**B**) ROS generation in HepG2 cells after various treatments as determined by FCM analysis. (**C**) Amount of ROS produced. (**D–E**) Apoptosis rates of HepG2 cells treated with TPL/Ce6 NPs (equivalent to 20 nM TPL and 54 nM Ce6) for 48 h using Annexin V-FITC/PI double staining by FCM analysis. ***p < 0.001 and **p < 0.01 indicates a statistically significant difference between the groups.

induction. However, TPL/Ce6 NPs demonstrated a significantly improved pro-apoptotic capacity over the free drugs. In a pH/ ROS-responsive medium (pH 5.8, 10 mM H_2O_2), TPL/Ce6 NPs induced a significantly higher rate of apoptosis compared to a neutral medium (pH 7.4), achieving a 2.6-fold increase (Figure 3E). These findings suggest that TPL/Ce6 NPs, responding to dual pH/ROS stimuli, significantly enhanced cytotoxicity, ROS production, and apoptosis in HepG2 cells through a combination of chemotherapy and photodynamic therapy.

Distribution of TPL/Ce6 NPs in vivo

To further explore the tumor tissue accumulation advantage of TPL/Ce6 NPs, we administered TPL/Ce6 NPs and free Ce6 (with an equivalent Ce6 dose of 4 mg/kg) to H22 tumor-bearing nude mice via tail vein injection, considering the autofluorescence of Ce6 under excitation. Figure 4A demonstrates that minimal fluorescence was detected in tumor tissues 24 h after free Ce6 injection, with predominant accumulation in the liver tissue. In contrast, significant fluorescence was observed in the tumor site as early as 2 h after administering TPL/Ce6 NPs, with strong fluorescence
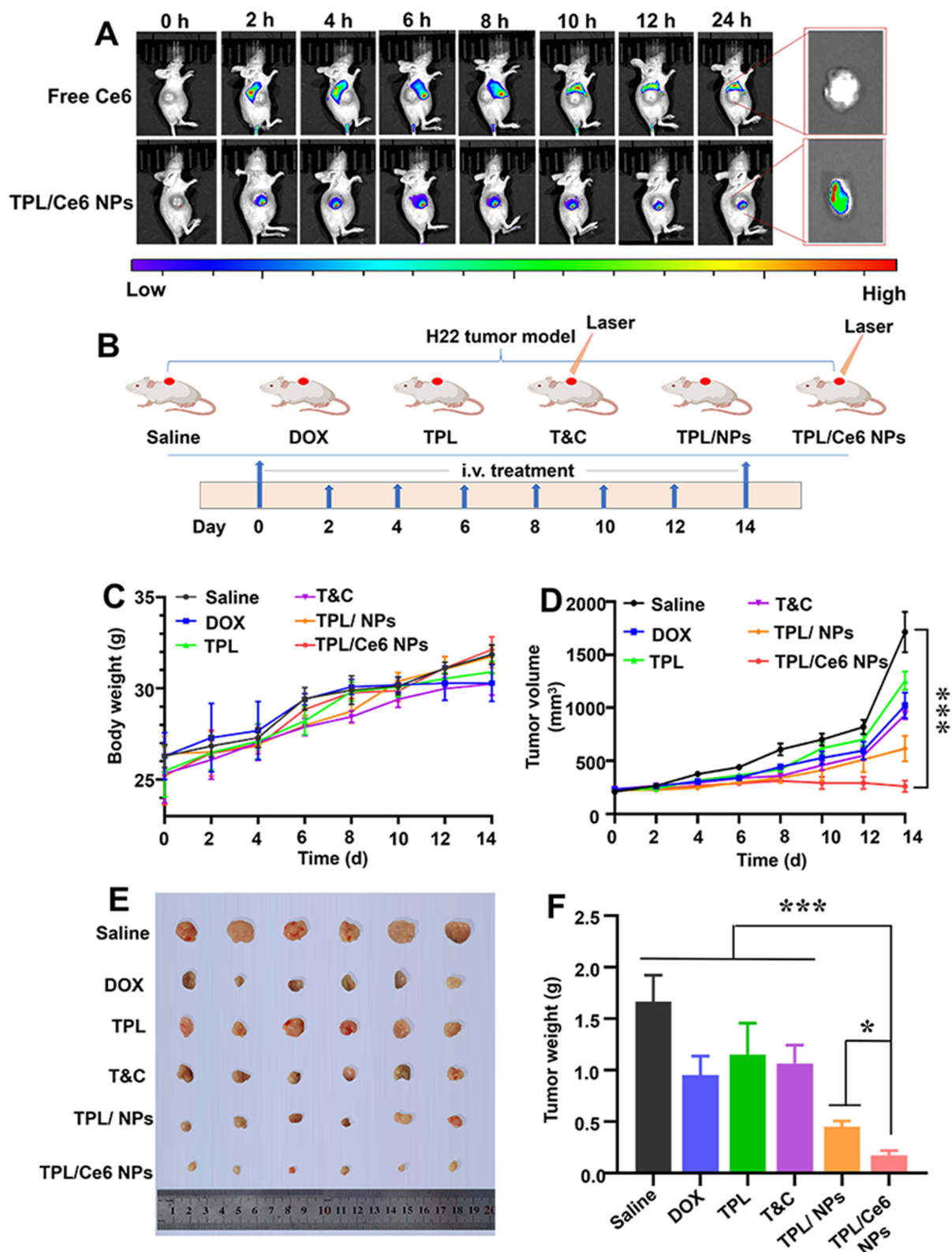
Figure 4 (**A**) In vivo real-time imaging of H22 tumor-bearing mice after intravenous injection of TPL/Ce6 NPs or free Ce6 at different time intervals, as well as the harvested tumor tissue at 24 h post-injection by ex vivo fluorescent imaging. (**B**) Experimental design of anti-tumor effects of TPL/Ce6 NPs on H22-bearing tumor mice model. Body weight changes (**C**) and tumor growth curves (**D**) of H22 tumor-bearing mice in the whole experiment period. (**E**) Representative photographs of tumors excised from each group on Day 14. (**F**) Statistical data of the harvested tumor tissue weight. Doxorubicin (DOX) was employed as the positive control. ***$p < 0.001$ and *$p < 0.05$ indicates a statistically significant difference between groups.

persisting up to 24 h post-injection. The marked difference in fluorescence intensity in the collected tumor tissues 24 h post-injection clearly showcased the tumor targeting superiority of mPEG-$_{TK}$-PBAE NPs, suggesting that the payload of mPEG-$_{TK}$-PBAE NPs could significantly enhance tumor accumulation, potentially leading to improved antitumor efficacy.

In vivo Chemo-Photodynamic Therapy of TPL/Ce6 NPs

The in vivo antitumor efficacy of TPL/Ce6 NPs was evaluated using a subcutaneous H22 tumor-bearing mouse model. As depicted in Figure 4B, treatments, including saline, DOX, free TPL, free TPL+Ce6 (T&C), TPL/NPs without Ce6, and TPL/Ce6 NPs, were administered bi-daily. DOX (2 mg/kg) served as a positive control. Initially, body weight trends throughout the study period suggested that continuous administration of DOX, free TPL, and TPL+Ce6 combinations led to systemic toxicity, evidenced by a reduction in body weight from day 12 onwards. Conversely, the nanoparticle formulations showed greater biosafety, as indicated by a body weight progression similar to the control group (Figure 4C). The antitumor outcomes (Figure 4D–F) highlighted the superior tumor suppression capability of TPL/Ce6 NPs over other treatments, including DOX. Free TPL (0.3 mg/kg) was ineffective in curtailing tumor growth. By day 12, a marked increase in tumor size was observed in the free TPL group; however, TPL/Ce6 NPs treatment markedly inhibited tumor growth. By day 14, tumor volume in the TPL/Ce6 NPs group was significantly reduced, comparable to the initial tumor size. Although DOX administration reduced tumor size, TPL/Ce6 NPs, containing 0.3 mg/kg of TPL and 4 mg/kg of Ce6, demonstrated a more potent tumor inhibitory effect. Hence, through the synergistic application of chemotherapy and photodynamic therapy via pH/ROS dual-responsive nanocarrier co-delivery, tumor size was effectively maintained at a minimum, with reduced tumor weight.

Potential Anti-Tumor Mechanisms of TPL/Ce6 NPs

Further analysis of the antitumor benefits of TPL/Ce6 NPs was conducted using IHC analysis. H&E staining revealed that, compared to the other groups, TPL/Ce6 NPs led to increased inflammatory infiltration and tumor necrosis (Figure 5A). Tumor biomarker expression levels further corroborated the enhanced antitumor effect of TPL/Ce6 NPs (Figure 5A–B). In the Ki67 indicator graph, the brown particles pointed by the red arrow represent positive Ki67 expression. The diminished Ki67 intensity in the TPL/Ce6 NPs group indicated suppressed cell proliferation. Elevated Bax levels and reduced Bcl-2 expression suggested the pro-apoptotic impact of TPL/Ce6 NPs on tumor cells. In the CD31 indicator graph, the brown particles pointed by the red arrow represent positive CD31 expression. The results showed that CD31 positive expression was lowest in TPL/Ce6 NPs group compared other group. The significantly lower levels of VEGF and CD31 served as indicators of the treatment's ability to effectively curb neovascularization within the tumor. These results underscored the potent tumor growth inhibition by TPL/Ce6 NPs in the H22 tumor-bearing mouse model.

Moreover, given the reduced body weight loss with TPL/Ce6 NPs compared to either free TPL or DOX treatments, biosafety was further assessed through H&E staining of mouse organs and evaluation of blood ALT and AST levels. Figure 6A indicated that, unlike liver histological damage caused by free TPL, TPL/Ce6 NPs did not induce pathological changes in the heart, liver, spleen, lung, and kidney. Blood ALT and AST levels were significantly elevated in the free TPL group (Figure 6B–E). However, no significant alterations were observed in the TPL/Ce6 NPs group in comparison to the control group, demonstrating the high biosafety profile of TPL/Ce6 NPs during treatment.

Discussion

Triptolide (TPL), a diterpenoid isolated from *Tripterygium wilfordii* Hook. F., possesses significant pharmacological properties. Modern pharmacological research has highlighted TPL's prominent anti-inflammatory, immunosuppressive, antitumor, and other critical biological activities, positioning it as a leading candidate for the next "blockbuster" drug.[27] Recent studies have demonstrated TPL's broad-spectrum antitumor and sensitizing effects, offering potential therapeutic benefits for various cancers, including hepatocellular carcinoma, lung cancer, and pancreatic cancer. Its antitumor mechanism is primarily through potent cytotoxicity, inducing apoptosis, overcoming drug resistance, and inhibiting both neovascularization and tumor metastasis.[5,28,29] However, its clinical application is limited by its reproductive toxicity and narrow therapeutic window.[30] Efforts to mitigate TPL's toxicity have included derivatization, nanodelivery, and combination with other drugs. Li et al developed a biomimetic nanosystem using cancer cell-platelet (PLT) hybrid
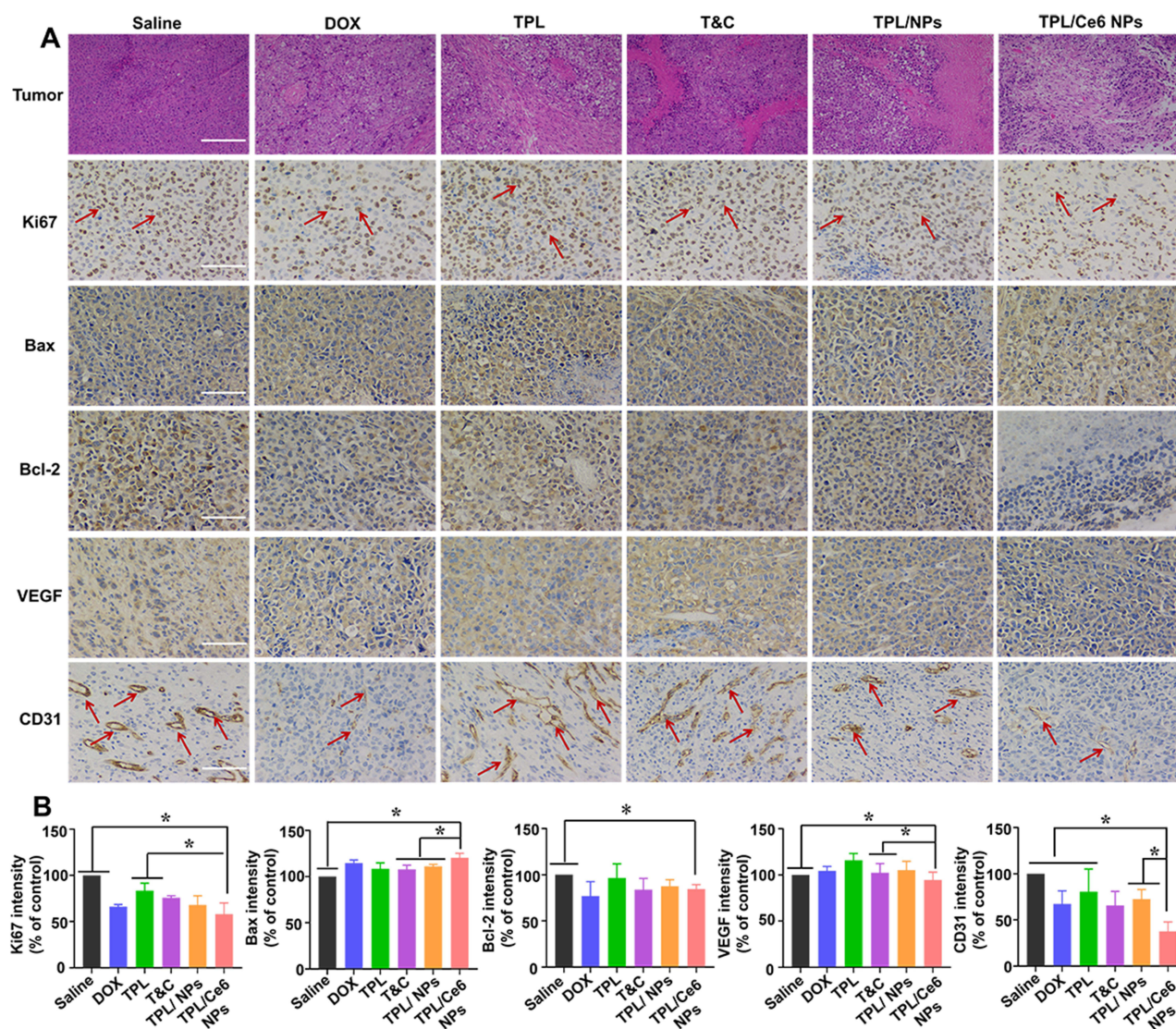
Figure 5 Immunohistochemical (IHC) staining of tumor tissues from H22-bearing tumor mice treated with various formulations. (**A**) H&E and IHC staining for Ki67 (the brown particles pointed by the red arrow represent positive Ki67 expression), Bax, Bcl-2, CD31 (the brown particles pointed by the red arrow represent positive CD31 expression) and VEGF (brown represents positive expression and blue represents cell nucleus). The scale bar is 50 μm. (**B**) Semi-quantitative analysis of Ki67, Bax, Bcl-2, VEGF, and CD31 positive expression levels was implemented by ImageJ software. *p < 0.05 indicates a statistically significant difference between the groups.

membrane camouflage for co-delivering sorafenib and TPL in hepatocellular carcinoma treatment.[31] Additionally, lipophilic cations such as triphenylphosphonium and E-4-(1H-indol-3-yl vinyl)-N-methylpyridinium iodide (F16) have been modified on TPL for tumor therapy, aiming to reduce toxicity.[32] However, combining TPL with other chemotherapy or cytotoxic drugs might exacerbate TPL's side effects. Conversely, photodynamic therapy (PDT), a minimally invasive technique that employs photosensitizers and specific light wavelengths to generate reactive oxygen species for inducing cell death,[33] offers precise tumor targeting while sparing normal tissues, thus enhancing safety when combined with TPL.[34–36] Thereby, it is more safety to combine TPL and PDT. Derivatization of compounds, while effective, often faces challenges such as complex processes and high costs. In this study, we have engineered TPL for use with PDT through a self-amplifying pH/ROS dual-responsive nanovesicle composed of PBAE-based copolymers, mPEG-$_{TK}$-PBAE, to co-deliver TPL and Ce6 (TPL/Ce6 NPs).

In our research on cellular uptake and biological distribution, we evaluated the differences and advantages between drugs in encapsulated (TPL/Ce6) and free forms. However, direct observation of TPL's cellular uptake and in vivo behavior is challenging, as TPL lacks the fluorescence properties of Ce6. Consequently, we plan to investigate the
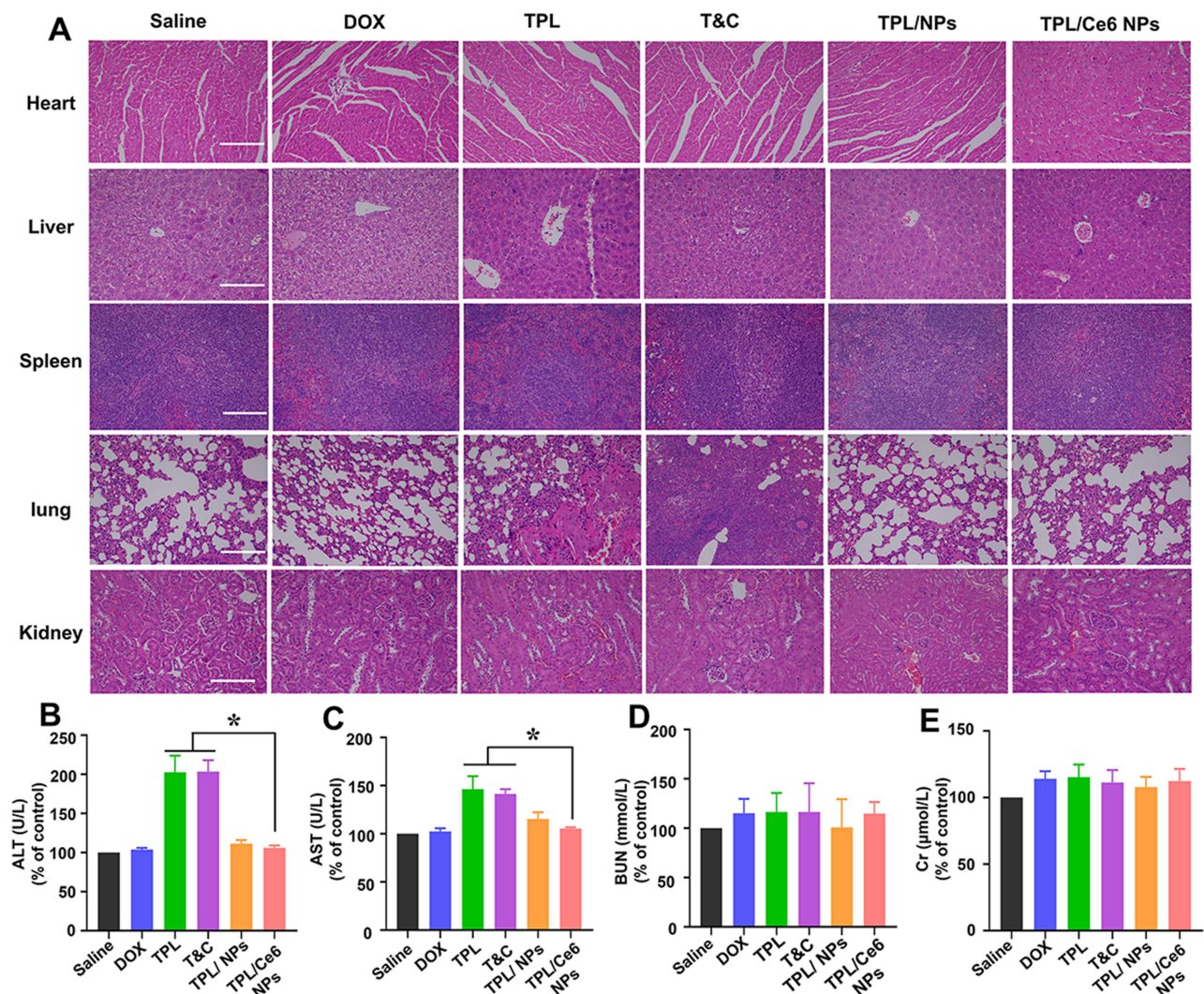
Figure 6 Histological analyses of main organs and blood biochemical indexes derived from H22-bearing tumor mice. (**A**) H&E histological analyses of main organs after various treatments of the H22 tumor model. The content of ALT (**B**), AST (**C**), BUN (**D**), and Cr (**E**) in blood after treatment. The scale bar is 50 μm. *$p < 0.05$ indicates a statistically significant difference between groups.

cellular uptake and distribution metabolism of TPL in both its free and nanoformulated states using classical pharmacokinetic research methods in future studies.

Given the instability of endogenous ROS in tumor cells, relying solely on the tumor's ROS for the rapid release of ROS in response to nanoparticles is inadequate. Thus, a self-amplified strategy, based on the initial ROS-responsive nanoparticle design, can be developed by augmenting the ROS content within tumor tissue, thereby enhancing the release response of the nanoparticles and their antitumor efficacy. For instance, Wang et al developed a targeted, self-enhanced ROS-responsive artesunatum prodrug nanoassembly for treating cervical cancer.[25] In our study, we leveraged the significantly elevated ROS levels in tumor cells (up to 1000 times higher than in normal cells) and the acidic pH of tumor environments to create pH/ROS dual-responsive NPs for the co-delivery of TPL and Ce6. Notably, the heterogeneity of tumors, including variations within different regions of tumor tissue and across different stages of tumor cells, leads to fluctuating levels of endogenous ROS. Here, the ROS generated by Ce6 acts to further accelerate payload release, functioning as a ROS amplifier. Consequently, the TPL/Ce6 NPs we developed are capable of enhancing anticancer outcomes synergistically by amplifying ROS-mediated drug release and cancer cell death.

Conclusion

In summary, we have successfully designed and synthesized a novel copolymer, mPEG-$_{TK}$-PBAE, through the Michael addition reaction. This copolymer forms pH/ROS dual-responsive nanoparticles for the co-delivery of TPL and Ce6 (TPL/Ce6 NPs), aiming for synergistic chemotherapy and PDT in HCC treatment. The TPL/Ce6 NPs, with an average particle size of 168.0±2.70 nm and a homogeneous spherical morphology, demonstrated precise and rapid drug release and $^1O_2$ production under light irradiation in acidic pH and ROS environments. In vitro, these NPs were efficiently internalized by HepG2 cells, showing a significantly enhanced therapeutic effect against cell proliferation, ROS generation, and apoptosis induction. More importantly, the advantages of tumor tissue accumulation, even 24 h post-administration, along with pH/ROS dual-responsive drug release, chemotherapy, and PDT, allowed the intravenous administration of TPL/Ce6 NPs to effectively suppress tumor growth in H22 tumor-bearing mice with high biosafety. Collectively, the designed TPL/Ce6 NPs hold promise as a co-delivery carrier for combined chemo-photodynamic therapy, offering a novel strategy to achieve amplified synergistic effects in cancer treatment.

Abbreviations

Ce6, chlorin e6; TPL, triptolide; mPEG-$_{TK}$-PBAE, methoxy poly (ethylene glycol)-thioketals-poly (β-amino esters); PDT, photodynamic therapy; $^1O_2$, cytotoxic oxygen; ROS, reactive oxygen species; HCC, hepatocellular Carcinoma; EPR, enhanced permeability and retention effect; GPC, gel permeation chromatography; HPLC, high-performance liquid chromatography; CLSM, confocal laser scanning microscopy; TEM, transmission electron microscopy; FTIR, Fourier transform infrared spectroscopy; H&E, hematoxylin and eosin; ALT, Alanine aminotransferase; AST, aspartate amino-transferase; BUN, urea nitrogen; Cr, creatinine; MMP, mitochondrial membrane potential.

Acknowledgments

Disclosure

The authors report no conflicts of interest in this work.

References

1. Xu J, Zheng Q, Cheng X, et al. Chemo-photodynamic therapy with light-triggered disassembly of theranostic nanoplatform in combination with checkpoint blockade for immunotherapy of hepatocellular carcinoma. *J Nanobiotechnology*. 2021;19(1):355. doi:10.1186/s12951-021-01101-1

2. Abuduwaili W, Wang X, Huang AT, et al. Iridium complex-loaded sorafenib nanocomposites for synergistic chemo-photodynamic therapy of hepatocellular carcinoma. *ACS Appl Mater Interfaces*. 2022;14(33):37356–37368. doi:10.1021/acsami.2c07247

3. Xie J, Wang Y, Choi W, et al. Overcoming barriers in photodynamic therapy harnessing nano-formulation strategies. *Chem Soc Rev*. 2021;50 (16):9152–9201. doi:10.1039/d0cs01370f

4. Li SG, Shi QW, Yuan LY, et al. C-Myc-dependent repression of two oncogenic miRNA clusters contributes to triptolide-induced cell death in hepatocellular carcinoma cells. *J Exp Clin Cancer Res*. 2018;37(1):51. doi:10.1186/s13046-018-0698-2

5. Zhang YQ, Shen Y, Liao MM, et al. Galactosylated chitosan triptolide nanoparticles for overcoming hepatocellular carcinoma: enhanced therapeutic efficacy, low toxicity, and validated network regulatory mechanisms. *Nanomedicine*. 2019;15(1):86–97. doi:10.1016/j.nano.2018.09.002

6. Ling D, Xia H, Park W, et al. pH-sensitive nanoformulated triptolide as a targeted therapeutic strategy for hepatocellular carcinoma. *ACS Nano*. 2014;8(8):8027–8039. doi:10.1021/nn502074x

7. Zhao X, Liu X, Zhang P, et al. Injectable peptide hydrogel as intraperitoneal triptolide depot for the treatment of orthotopic hepatocellular carcinoma. *Acta Pharm Sin B*. 2019;9(5):1050–1060. doi:10.1016/j.apsb.2019.06.001

8. Sun R, Dai J, Ling M, Yu L, Yu Z, Tang L. Delivery of triptolide: a combination of traditional Chinese medicine and nanomedicine. *J Nanobiotechnology*. 2022;20(1):194. doi:10.1186/s12951-022-01389-7

9. Alsaied OA, Sangwan V, Banerjee S, et al. Sorafenib and triptolide as combination therapy for hepatocellular carcinoma. *Surgery*. 2014;156 (2):270–279. doi:10.1016/j.surg.2014.04.055

10. Zhao Y, Gu Y, Qi F, et al. Engineering adipocytes for targeting delivery of triptolide derivative and Ce6 for malignant melanoma cytotoxic-PDT synergistic strategy[J]. *Mater Design*. 2023;228:111860 doi:10.1016/j.matdes.2023.111860

11. Yu L, Wang Z, Mo Z, et al. Synergetic delivery of triptolide and Ce6 with light-activatable liposomes for efficient hepatocellular carcinoma therapy. *Acta Pharm Sin B*. 2021;11(7):2004–2015. doi:10.1016/j.apsb.2021.02.001

12. Aghizadeh B, Taranejoo S, Monemian SA, et al. Classification of stimuli-responsive polymers as anticancer drug delivery systems. *Drug Deliv*. 2015;22(2):145–155. doi:10.3109/10717544.2014.887157

13. Alshememry AK, El-Tokhy SS, Unsworth LD. Using properties of tumor microenvironments for controlling local, on-demand delivery from biopolymer-based nanocarriers. *Curr Pharm Des*. 2017;23(35):5358–5391. doi:10.2174/1381612823666170522100545

14. Peng S, Xiao F, Chen M, Gao H. Tumor-microenvironment-responsive nanomedicine for enhanced cancer immunotherapy. *Adv Sci*. 2022;9(1): e2103836. doi:10.1002/advs.202103836

15. Shi J, Ren Y, Ma J, et al. Novel CD44-targeting and pH/redox-dual-stimuli-responsive core-shell nanoparticles loading triptolide combats breast cancer growth and lung metastasis. *J Nanobiotechnology*. 2021;19(1):188. doi:10.1186/s12951-021-00934-0

16. Wu Y, Li J, Zhong X, et al. A pH-sensitive supramolecular nanosystem with chlorin e6 and triptolide co-delivery for chemo-photodynamic combination therapy. *Asian J Pharm Sci*. 2022;17(2):206–218. doi:10.1016/j.ajps.2021.12.003

17. Liu N, Wu L, Zuo W, et al. pH/Thermal-sensitive nanoplatform capable of on-demand specific release to potentiate drug delivery and combinational Hyperthermia/Chemo/Chemodynamic Therapy. *ACS Appl Mater Interfaces*. 2022;14(26):29668–29678. doi:10.1021/acsami.2c09685

18. Wang H, Gao Z, Jiao D, et al. A microenvironment dual-responsive nano-drug equipped with PD-L1 blocking peptide triggers immunogenic pyroptosis for prostate cancer self-synergistic immunotherapy. *Adv Funct Mater*. 2023;33(16):2214499. doi:10.1002/adfm.202214499

19. Zhang S, Guo N, Wan G, et al. pH and redox dual-responsive nanoparticles based on disulfide-containing poly (β-amino ester) for combining chemotherapy and COX-2 inhibitor to overcome drug resistance in breast cancer. *J Nanobiotechnology*. 2019;17(1):109. doi:10.1186/s12951-019-0540-9

20. Yin TJ, Wang YY, Chu XX, et al. Free adriamycin-loaded pH/reduction dual-responsive hyaluronic acid-adriamycin prodrug micelles for efficient cancer therapy. *ACS Appl Mater Interfaces*. 2018;10(42):35693–35704. doi:10.1021/acsami.8b09342

21. Zhang Y, Li Y, Tian H, et al. Redox-responsive and dual-targeting hyaluronic acid-methotrexate prodrug self-assembling nanoparticles for enhancing intracellular drug self-delivery. *Mol Pharm*. 2019;16(07):3133–3144. doi:10.1021/acs.molpharmaceut.9b00359

22. Feng Y, Xie X, Zhang H, et al. Multistage-responsive nanovehicle to improve tumor penetration for dual-modality imaging-guided photodynamic-immunotherapy. *Biomaterials*. 2021;275:120990. doi:10.1016/j.biomaterials.2021.120990

23. Lin C, He H, Zhang Y, et al. Acetaldehyde-modified-cystine functionalized ZrMOFs for pH/GSH dual-responsive drug delivery and selective visualization of GSH in living cells. *RSC Adv*. 2020;10(6):3084–3091. doi:10.1039/C9RA05741B

24. Cheung EC, Vousden KH. The role of ROS in tumour development and progression. *Nat Rev Cancer*. 2022;22(5):280–297. doi:10.1038/s41568-021-00435-0

25. Wang S, Yu K, Yu Z, et al. Targeting self-enhanced ROS-responsive artesunatum prodrug nanoassembly potentiates gemcitabine activity by down-regulating CDA expression in cervical cancer[J]. *Chinese Chem Lett*. 2023;34(7):108184 doi:10.1016/j.cclet.2023.108184

26. Niu W, Wang J, Wang Q, Shen J. Celastrol loaded nanoparticles with ROS-response and ros-inducer for the treatment of ovarian cancer. *Front Chem*. 2020;8:574614. doi:10.3389/fchem.2020.574614

27. Zhu D, Zhang Q, Chen Y, et al. Mechanochemical preparation of triptolide-loaded self-micelle solid dispersion with enhanced oral bioavailability and improved anti-tumor activity. *Drug Deliv*. 2022;29(1):1398–1408. doi:10.1080/10717544.2022.2069879

28. Kim ST, Kim SY, Lee J, et al. Triptolide as a novel agent in pancreatic cancer: the validation using patient derived pancreatic tumor cell line. *BMC Cancer*. 2018;18(1):1103. doi:10.1186/s12885-018-4995-0

29. Wei YM, Wang YH, Xue HQ, Luan ZH, Liu BW, Ren JH. Triptolide, A Potential Autophagy Modulator. *Chin J Integr Med*. 2019;25(3):233–240 doi:10.1007/s11655-018-2847-z

30. Xi C, Peng S, Wu Z, Zhou Q, Zhou J. Toxicity of triptolide and the molecular mechanisms involved. *Biomed Pharmacother*. 2017;90:531–541. doi:10.1016/j.biopha.2017.04.003

31. Li Z, Yang G, Han L, Wang R, Gong C, Yuan Y. Sorafenib and triptolide loaded cancer cell-platelet hybrid membrane-camouflaged liquid crystalline lipid nanoparticles for the treatment of hepatocellular carcinoma. *J Nanobiotechnology*. 2021;19(1):360. doi:10.1186/s12951-021-01095-w

32. Xing W, Liu G, Zhang Y, Zhang T, Lou H, Fan P. Selective antitumor effect and lower toxicity of mitochondrion-targeting derivatization of triptolide. *J Med Chem*. 2024;67(2):1093–1114. doi:10.1021/acs.jmedchem.3c01508

33. Ruiz-González R, Milán P, Bresolí-Obach R, et al. Photodynamic synergistic effect of pheophorbide a and doxorubicin in combined treatment against tumoral cells. *Cancers*. 2017;9(2):18. doi:10.3390/cancers9020018

34. Zhou Z, Song J, Nie L, Chen X. Reactive oxygen species generating systems meeting challenges of photodynamic cancer therapy. *Chem Soc Rev*. 2016;45(23):6597–6626. doi:10.1039/c6cs00271d

35. Lovell JF, Liu TW, Chen J, Zheng G. Activatable photosensitizers for imaging and therapy. *Chem Rev*. 2010;110(5):2839–2857. doi:10.1021/cr900236h

36. Kessel D. Photodynamic therapy: apoptosis, paraptosis and beyond. *Apoptosis*. 2020;25(09–10):611–615. doi:10.1007/s10495-020-01634-0